Surface & Coatings Technology 230 (2013) 202–207

Contents lists available at SciVerse ScienceDirect

Surface & Coatings Technology

journal homepage: www.elsevier.com/locate/surfcoat

Vapor-deposited hydrogenated and oxygen-deficient molybdenum oxide thin films for application in organic optoelectronics ☆

Maria Vasilopoulou [a,*], Ioannis Kostis [a,b], Antonios M. Douvas [a], Dimitra G. Georgiadou [a], Anastasia Soultati [a], Giorgos Papadimitropoulos [a], Nikos A. Stathopoulos [b], Stelios S. Savaidis [b], Panagiotis Argitis [a], Dimitris Davazoglou [a]

[a] NCSR "Demokritos," Institute of Microelectronics, PO Box 60228, 15310 Agia Paraskevi, Attiki, Greece
[b] Department of Electronics, Technological and Educational Institute of Pireaus, 12244 Aegaleo, Greece

ARTICLE INFO

Available online 1 June 2013

Keywords:
Vapor-deposited molybdenum oxides
Oxygen deficient
Hydrogenated
Organic optoelectronics

ABSTRACT

Vapor-deposited molybdenum oxide films are used as low resistance anode interfacial layers in applications such as organic light emitting diodes (OLEDs) and organic photovoltaics (OPVs). A versatile method for the vapor deposition of molybdenum oxide layers is presented, which offers the control of the oxygen stoichiometry of the deposited films and their doping with hydrogen. The possibility of tuning the electronic structure of the deposited molybdenum oxides is also investigated by controlling oxygen deficiency and hydrogenation (the incorporation of hydrogen within the molybdenum oxide's lattice). To take advantage of the altered electronic properties of the non-stoichiometric Mo oxides, we embedded them as anode interfacial layers in organic optoelectronic devices. Large improvement in the operational characteristics of both electroluminescent devices and bulk heterojunction solar cells was achieved and correlated with the oxygen deficiency and the hydrogen content of the Mo oxides.

© 2013 The Authors. Published by Elsevier B.V. Open access under CC BY-NC-ND license.

1. Introduction

Transition metal oxides (TMOs) have been recognized as one of the most promising class of materials that are widely used in organic optoelectronic devices to enhance charge exchange with organic molecules [1–6]. Molybdenum trioxide (MoO_3), in particular, has drawn considerable attention because of the improvement induced in the performance of organic light emitting diodes (OLEDs) and organic photovoltaics (OPVs) when inserted as hole injection layer in these devices [7–15]. This improvement has been mainly attributed to the decrease of the hole injection/extraction barrier at the anode/organic interfaces. The lowering of the charge injection/extraction barrier has been considered to be a result of favorable energy level alignment between the MoO_3 and the organic semiconducting molecules [16]. This is due to the oxide's high work function value that allows facile charge transfer to/from the highest occupied molecular orbital (HOMO) of an organic molecule. In general, the work function is an important parameter for charge exchange because it represents the energetic requirements for adding or removing an electron to or from a solid. In recent years, substoichiometric molybdenum oxides (MoO_x, $x < 3$), formed mainly by thermal evaporation, were also used to enhance hole exchange in OLEDs and OPVs mainly due to their improved *n*-type conductivity originated from intrinsic oxygen vacancies [17–22].

Our group has recently investigated the electronic structures of tungsten (W) and molybdenum (Mo) oxide films deposited in reducing environments (termed as substoichiometric metal oxide films) and their application as charge transport layers in organic optoelectronic devices [9–11,23]. In this work, we used a simple, cost-effective method to prepare oxygen-deficient and hydrogenated molybdenum oxides and to clarify their role in organic optoelectronic devices. We present evidence that both oxygen deficiency and hydrogenation result in occupation of occupied gap states lying within the forbidden gap. Upon the implementation of oxygen-deficient and hydrogenated Mo oxides as hole injection/extraction layers in poly [(9,9-dioctylfluorenyl-2,7-diyl)-co-(1,4-benzo-{2,1′,3}-thiadiazole)]

* Corresponding author at: NCSR "Demokritos," Institute of Microelectronics, PO Box 60228, 15310 Agia Paraskevi, Attiki, Greece. Tel.: +30 210 6503269; fax: +30 210 6511723.
E-mail address: mariva@imel.demokritos.gr (M. Vasilopoulou).

0257-8972 © 2013 The Authors. Published by Elsevier B.V. Open access under CC BY-NC-ND license.
http://dx.doi.org/10.1016/j.surfcoat.2013.05.033

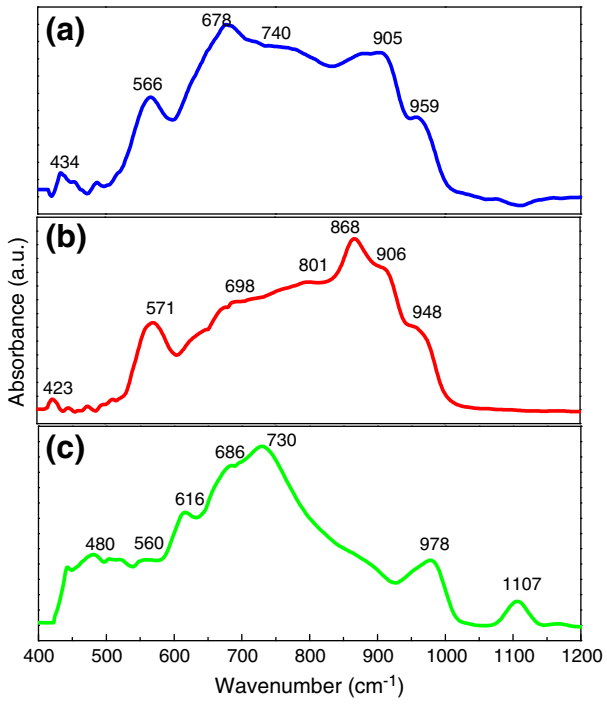

Fig. 1. FT-IR spectra of molybdenum oxide films: (a) MoO_3, (b) MoO_{3-x}, and (c) H_yMoO_{3-x}, deposited in O_2, N_2, and H_2 environment, respectively.

(F8BT)-based OLEDs and poly(3-hexythiophene) (P3HT):[6,6]-phenyl-C71-butyric acid methyl ester (PCBM-71),(P3HT:PCBM-71) bulk heterojunction OPVs, improved device performance was achieved compared to devices with stoichiometric MoO_3.

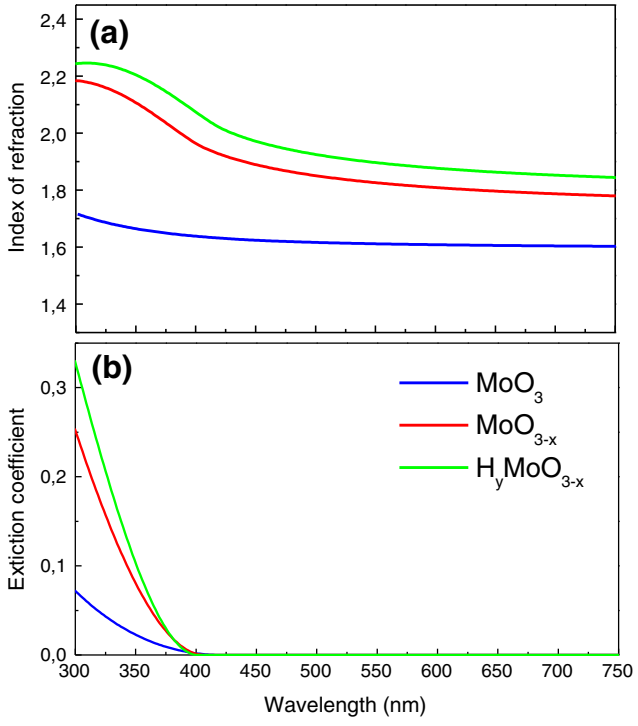

Fig. 2. Wavelength variation of the (a) refractive index and (b) the extinction coefficient of Mo oxide films with a thickness of 10 nm.

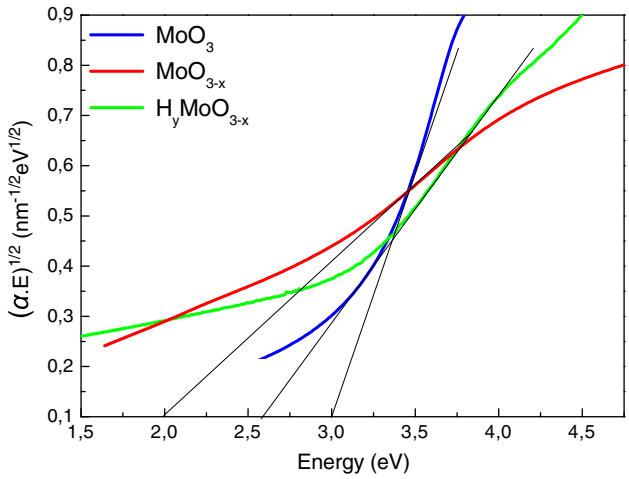

Fig. 3. Tauc plot $(\alpha(h\nu)^{1/2}$ versus $h\nu)$ derived from absorption measurements for 10-nm-thick Mo oxide films.

2. Experimental

2.1. Materials preparation and characterization

Stoichiometric MoO_3, oxygen-deficient, MoO_{3-x} (reduced in nitrogen environment), and hydrogenated, H_yMoO_{3-x} (reduced in hydrogen environment) films, were deposited in a homemade system, consisting of a stainless steel reactor, similar to the one previously presented [24,25]. The samples were positioned on an aluminum susceptor, 2.5 cm below a Mo filament heated by an (AC) current flowing through two Cu leads. The pressure in the reactor (base pressure) was set by a diaphragm pressure gauge (Baratron) and a PC-driven needle valve allowing the flow of O_2, N_2, or pure hydrogen through the reactor and thus setting the base pressure at the desired value. For the deposition, after loading the substrate, the reactor was evacuated down to 10^{-2} Torr. Then, the Mo wire was heated at 560 °C. The deposition rate was measured about 0.5 nm/s in the case of the stoichiometric and oxygen-deficient films, while it was found ~0.25 nm/s for the hydrogenated Mo oxides. During deposition, the substrates remained at near room temperature, depending on the deposition time, however, never exceeding 50 °C. Transmittance and absorption measurements were performed using a Perkin Elmer Lampda 40 UV/Vis spectrophotometer. FT-IR transmittance spectra were recorded on a Bruker, Tensor 27 spectrometer using 128 scans at 4 cm^{-1}. The film resistance was measured using the four-point probe method with a dedicated Keithley meter. A LEO Supra 35 VP scanning electron (SEM) and a PHILIPS CM 20 transmission electron (TEM) microscope were used for film surface and bulk characterization, respectively. The dispersion of the refractive indices and extinction coefficients were measured using a J. A. Woollam Inc. M2000F rotating compensator ellipsometer (RCE™) running the WVASE32 software at an angle of incidence of 75.14°.

2.2. Devices fabrication and characterization

OLEDs and OPVs were fabricated on ITO-coated glass substrates (2 × 2 cm) with a sheet resistance 20 Ω/square, which served as the anode electrode. Substrates were ultrasonically cleaned with a standard solvent regiment (15 min each in acetone and isopropanol). In OLEDs, the Mo oxide layer was then deposited followed by an approximately 70-nm-thick emissive layer (EML), the green-emitting copolymer poly[(9,9-dioctylfluorenyl-2,7-diyl)-co-(1,4-benzo-{2,1′,3}-thiadiazole)] (F8BT), spin coated from a chloroform solution (at a

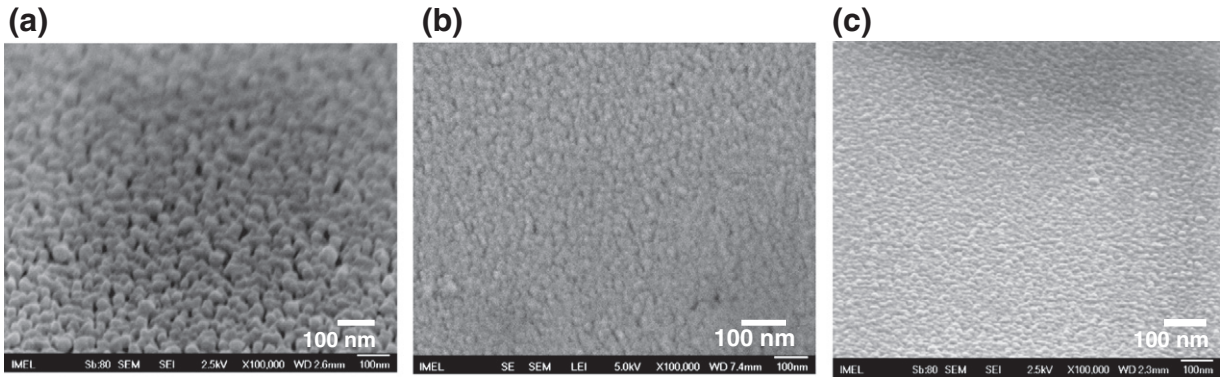

Fig. 4. SEM images of Mo oxides: (a) MoO_3, (b) MoO_{3-x}, and (c) H_yMoO_{3-x}, deposited in O_2, N_2, and H_2, respectively. The scale bar is at 100 nm.

concentration of 6 mg/ml). After deposition, the EML layer was annealed at 80 °C for 10 min in air. F8BT was purchased from American Dye Source and used as received. Then, in some devices, a previously reported thin polyoxometalate (POM) layer was deposited from a solution in methanol, on top of the EML to serve as an electron injection/transport layer [26,27]. The devices were completed with a 150-nm-thick aluminum cathode, deposited in a dedicated chamber. Films thicknesses were estimated with ellipsometry. For OPVs, the active layer was a blend (1:0.8 wt%) of poly(3-hexylthiophene) (P3HT) and [6,6]-phenyl-C71-butyric acid methyl ester (PCBM-71), spin coated from a 10-mg/ml chloroform solution to form a 100-nm-thick film. After deposition, the active layer was annealed at 125 °C for 10 min.

3. Results and discussion

The structural changes of the molybdenum oxide films deposited in different environments were studied with Fourier transform infrared (FTIR) spectroscopy. The results are shown in Fig. 1. Films deposited in oxygen environment were found to be fully stoichiometric (MoO_3, curve a) and showed three characteristic bands, which correspond to the three different kinds of oxygen bondings that exist in an octahedron of the thermodynamically stable orthorhombic structure of MoO_3: (a) two bands at 959 and 905 cm^{-1} attributed to the stretching mode of terminal oxygen (νO═Mo), (b) two bands at 740 and 678 cm^{-1} assigned to the stretching mode of doubly coordinated oxygen (νO–Mo_2), and (c) a band at 566 cm^{-1} attributed to the stretching mode of triply coordinated oxygen ($\nu O - Mo_3$) [28–30]. Upon introducing N_2 within the chamber the molybdenum oxide films were found substoichiometric (curve b); a shift of the νO–Mo_2 band to lower wave numbers (868 → 721 → 683 cm^{-1}) is detected, confirming therefore the reduction of the MoO_3 films possibly through the formation of oxygen vacancies in the doubly coordinated oxygen [20]. Similarly, the band of the νO═Mo shifts to higher wave numbers (948 → 973 → 975 cm^{-1}). In the case of the hydrogenated film (deposited in pure hydrogen environment) (curve c), the shift of the νO═Mo band is even higher (978 cm^{-1}), indicating that in that case the O═Mo bonds are more affected, possibly through the incorporation of hydrogen within the oxide's lattice (H-doping). As a consequence, a new band also appears at 1107 cm^{-1} attributed to the bending mode of Mo–OH bonds (δMo–OH); similar results have been reported in literature for molybdenum bronzes (H_xMoO_3) [31,32].

Spectroscopic ellipsometry (SE) measurements showed that for stoichiometric MoO_3 the dispersion of its refractive index was dependent on deposition time (i.e. film thickness) and that after 5 sec (i.e. 50-nm-thick films) of deposition, the refractive index decreased and obtained values below that of fused silica (1.45), as the film became highly porous. Oxygen-deficient and hydrogenated Mo oxide films showed increased refractive indices, n, and extinction coefficients, k, compared to those of MoO_3, as seen in Fig. 2a and b, respectively. These results, combined with data derived from X-ray (XPS) and ultraviolet (UPS) photoelectron spectroscopy published elsewhere [9–11], are clear evidence for the formation of gap states within the oxide's band gap after its reduction with N_2 and especially with H_2 [11]. As a result, different band gap values, E_G, were calculated for each Mo oxide. The E_G values were derived from the Tauc plots, presented in Fig. 3, as the intercept of the tangent in the plot of $\alpha(h\nu)^{1/2}$ versus $h\nu$ (where α is the absorption coefficient) with the $h\nu$ axis gives the band gap energy. Stoichiometric MoO_3 films have an optical band gap of approximately 3.0 eV, while both oxygen-deficient (MoO_{3-x}) and hydrogenated

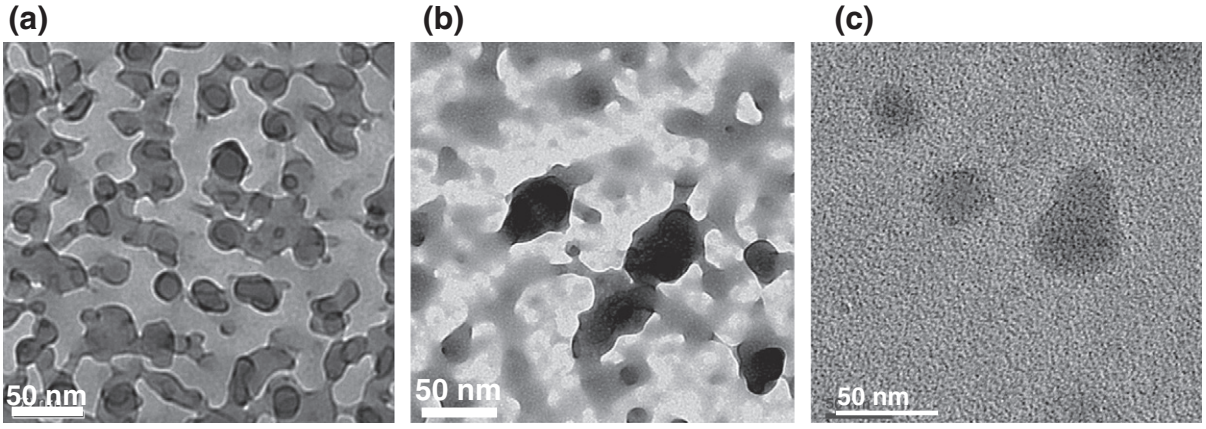

Fig. 5. TEM images of (a) MoO_3, (b) MoO_{3-x}, and (c) H_yMoO_{3-x} films. The scale bar is at 50 nm.

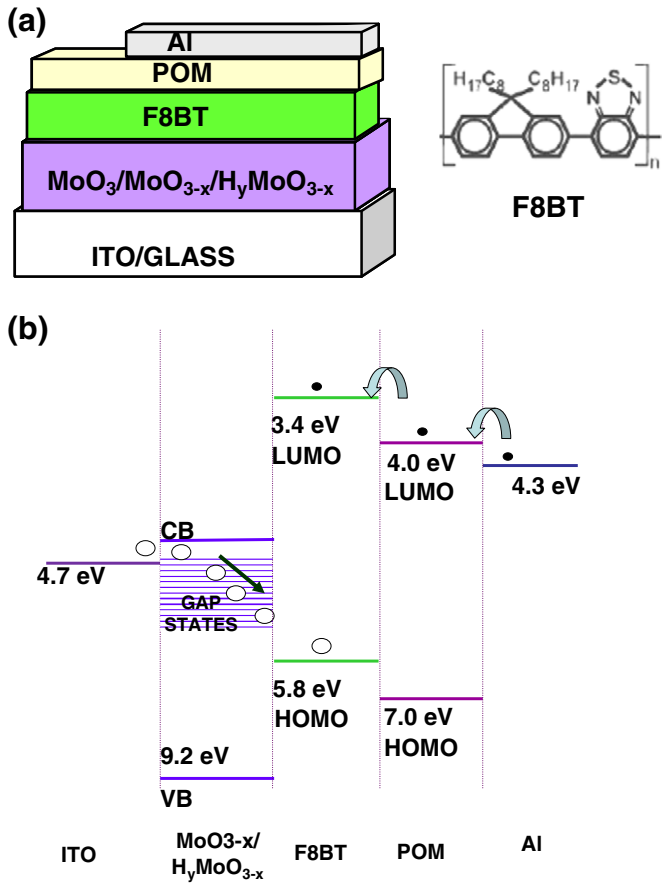

Fig. 6. (a) The OLED device architecture and the emissive layer (F8BT) chemical structure and (b) the corresponding energy diagram.

(H_yMoO_{3-x}) films exhibit smaller values due to the presence of the occupied gap states within their forbidden gap [11].

The morphology of these films comprises a grain-like, nanostructured surface as it can be seen in scanning electron microscopy (SEM) pictures, presented in Fig. 4. The stoichiometric film exhibited grains with dimensions around 30–35 nm. However, the grain size seems to substantially decrease when films are deposited in oxygen-poor environment; especially in the case of the hydrogenated one, the size of these grains is less than 5–10 nm. The porosity of the films is also decreasing upon hydrogenation, resulting in improved film forming properties (smoother layers with decreased surface roughness), which may be beneficial for device performance. We also used transmission electron microscopy (TEM) to characterize the structural evolution of the Mo oxides. The results are presented in Fig. 5. All films were completely amorphous. The stoichiometric and oxygen-deficient films (Fig. 5a and b) exhibited an obvious porosity with the porosity of the former to be larger than the porosity of the latter. The hydrogen-deposited Mo oxide film, however (Fig. 5c), exhibited the best homogeneity as it exhibited the lowest pinhole density, which contributes to the formation of a stable interface and is beneficial for device performance.

After having correlated the film preparation conditions with their electronic structure and properties, we then applied these oxides as anode interlayers in organic polymer-based organic light emitting diodes (OLEDs). The fabricated device structure was ITO/Mo oxide (hole injection layers)/F8BT (as the emissive layer)/polyoxometalate (POM) (electron injection layer)/Al. The device architecture and the emissive layer (F8BT) chemical structure are shown in Fig. 6a. In Fig. 6b, the corresponding energy diagram, as derived from UPS measurements [11], is illustrated. From this energy diagram, the formation of gap states within the substoichiometric or hydrogenated oxide's energy gap is evident. These states are expected to have a positive impact in the device operation as they can serve as paths to permit hole transport from the polymer's highest occupied molecular orbital (HOMO) to the anode, thus reducing the hole injection barrier at the ITO/F8BT interface.

In Fig. 7(a) the current density–voltage–luminance (J–V–L) characteristics for devices with a 5-nm-thin Mo oxide film are shown. In the MoO_3-based device, a rather large turn-on voltage (light-emission begins at about 3.5 V) and overall low performance (with maximum current density about 1700 mA/cm^2 and a peak luminance of 4000 cd/m^2) is observed. On the contrary, the oxygen-deficient and especially the hydrogenated Mo oxide-based devices exhibited more than one order of magnitude higher luminance, accompanied by a large decrease in the device turn-on and generally in the operating voltage. The device with the H_yMoO_{3-x} reaches luminance values up to 30000 cd/m^2 and current densities of 4300 A/m^2, while it also exhibits a low turn-on voltage of 2.5 V. The peak efficiency of 8 cd/A (Fig. 7(b)) represents one of the best values reported for OLEDs incorporating thin F8BT layers. It should be mentioned that the time stability of the devices operating in air was tested in a period of 700 h and was found satisfactory for all three different types of Mo oxide-based devices (data not shown) because of the exceptional environmental stability of the molybdenum oxide layers.

Finally, we investigate the effect of the incorporation of the Mo oxides described previously as hole extraction/transport (HEL/HTL) layers in OPVs based on P3HT:$PC_{71}BM$ (1:0.8 wt/%) bulk heterojunction (BHJ) photoactive layer. The beneficial use of thermally evaporated MoO_3 as anode buffer layer in OPVs has already been shown by other groups [33]; the purpose of this work was to demonstrate the benefits of deposition of Mo oxide layers in reducing environments. The device architecture is presented in Fig. 8(a), while the corresponding energy level diagram derived from UPS measurements [11] is also shown in

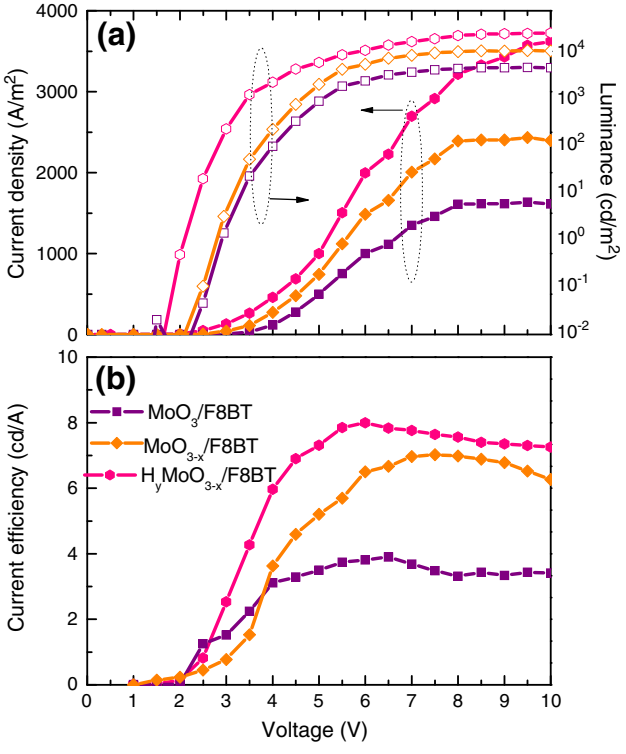

Fig. 7. (a) Current density–voltage (solid symbols) and luminance–voltage (open symbols) characteristic curves of OLEDs with the structure ITO/Mo oxides (5 nm)/F8BT/Al devices. (b) The corresponding current efficiency-voltage characteristics.

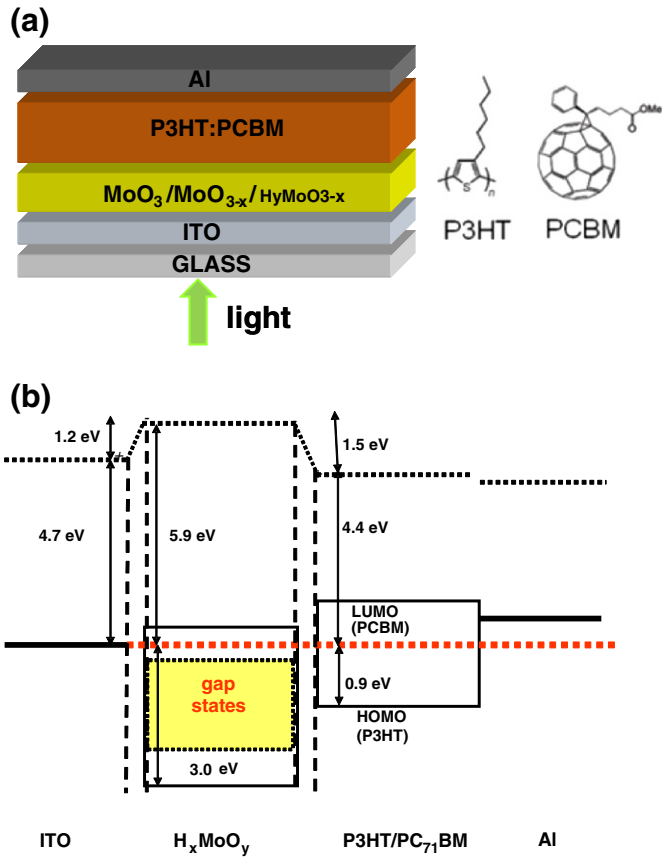

Fig. 8. (a) The OPV device architecture and (b) the corresponding energy diagram.

Fig. 8(b). It should be mentioned that the OPV devices are consisting of a simple aluminum cathode without an additional electron injection layer (as in the case of OLEDs described above). The Mo oxide thicknesses were optimized at 10 nm, while the photoactive layer was about 100 nm. All Mo oxide layers were exposed to air after their deposition and prior to BHJ layer spin coating, and thus, our devices' operation cannot be considered as optimized. Current density–voltage (*J*–*V*) characteristics under AM 1.5 G irradiation are shown in Fig. 9. A significant improvement in the short-circuit current (Jsc), the open-circuit voltage (Voc), the fill factor (FF), and the cell power conversion efficiency (PCE) was achieved for substoichiometric Mo oxides compared to the stoichiometric MoO_3 HEL. In particular, Voc increases from 0.52 V for MoO_3 to 0.59 V for MoO_{3-x} and even further to 0.64 V for H_yMoO_{3-x} film-based OPVs. Similarly, the Jsc increases from −5.7 to −7.3 and further to −8.0 mA/cm^2 for the MoO_3, MoO_{3-x} and H_yMoO_{3-x} bearing devices, respectively, while the FF increases from 0.32 to 0.54 (almost a 70% improvement) for the device with the stoichiometric and the devices with the non-stoichiometric Mo oxides, respectively. The large enhancement of the Voc, the Jsc, and the FF are attributed to the considerable reduction of the series resistance and the substoichiometric Mo oxide modified cells (from 50 Ω cm^2 for the MoO_3-based cell to 28 Ω cm^2 and even further to 10 Ω cm^2 for the MoO_{3-x} and the H_yMoO_{3-x} based cells, respectively), coming mainly from improved transport through the gap states, as illustrated in Fig. 8(b). In addition, the non-stoichiometric Mo oxides exhibited less adsorbed water (measured with FTIR, not shown), which may be destructive for device operation, as was verified by others for surface contaminants present in thermally air exposed MoO_3 [34,35].

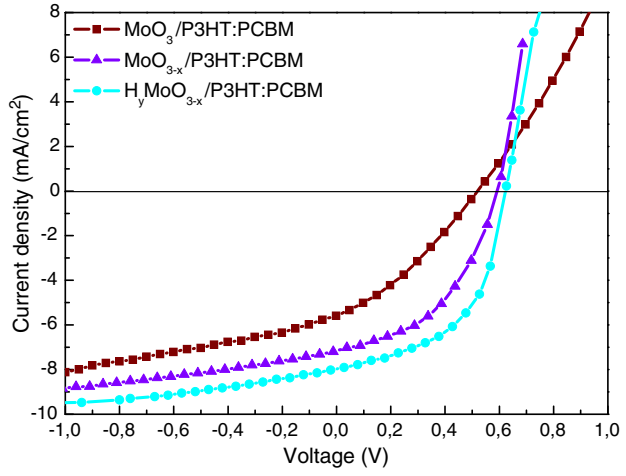

Fig. 9. Current density versus voltage characteristics for P3HT:$PC_{71}BM$ BHJ devices embedding 10 nm Mo oxide hole extracting layers.

4. Conclusions

In summary, we have shown that oxygen-deficient and hydrogenated Mo oxides exhibit desirable electronic properties, relative to their parent stoichiometric, for application in organic optoelectronic devices. The tuning of their electronic structure was achieved as a result of either oxygen deficiency or hydrogen incorporation within their lattice, evidenced through the hydroxyl group formation. Electrons from oxygen vacancies or from hydrogen dopant atoms are transferred to states located inside their band gap. As a consequence, a favorable energy alignment at the metal oxide/organic interface may occur. The beneficial role of hydrogenation versus oxygen vacancy formation in Mo oxides for application in efficient organic electronic devices was demonstrated.

Acknowledgments

This research has been co-financed by the European Union (European Social Fund – ESF) and Greek national funds through the Operational Program "Education and Lifelong Learning" of the National Strategic Reference Framework (NSRF)-Research Funding Program: ARCHIMEDES III. Investing in knowledge society through the European Social Fund.

References

[1] M.C. Gwinner, R. Di Pietro, Y. Vaynzof, K.J. Greenberg, P.K.H. Ho, R.H. Friend, H. Sirringhaus, Adv. Funct. Mater. 21 (2011) 1432.
[2] K. Morii, M. Ishida, T. Takashima, T. Shimoda, Q. Wang, K. Nazeeruddin, M. Grätzel, Appl. Phys. Lett. 89 (2006) 183510.
[3] M.T. Greiner, L. Chai, M.G. Helander, W.-M. Tang, Z.-H. Lu, Adv. Funct. Mater. 23 (2) (2013) 215.
[4] J. Meyer, S. Hamwi, S. Schmale, T. Winkler, H.-H. Johannes, T. Riedl, W. Kowalsky, J. Mater. Chem. 19 (2009) 702.
[5] M. Kröger, S. Hamwi, J. Meyer, T. Riedl, W. Kowalsky, A. Kahn, Org. Electron. 10 (2009) 932.
[6] S. Hamwi, J. Meyer, M. Kröger, T. Winkler, M. Witte, T. Riedl, A. Kahn, W. Kowalsky, Adv. Funct. Mater. 20 (2010) 1762.
[7] M.T. Greiner, M.G. Helander, W.-M. Tang, Z.-B. Wang, J. Qiu, Z.-H. Lu, Nat. Mater. 11 (2012) 76.
[8] M.T. Greiner, L. Chai, M.G. Helander, W.-M. Tang, Z.-H. Lu, Adv. Funct. Mater. 22 (11) (2012) 4557.
[9] M. Vasilopoulou, L.C. Palilis, D.G. Georgiadou, S. Kennou, I. Kostis, D. Davazoglou, P. Argitis, Appl. Phys. Lett. 100 (2012) 013311.
[10] M. Vasilopoulou, L.C. Palilis, D.G. Georgiadou, P. Argitis, S. Kennou, L. Syggelou, I. Kostis, G. Papadimitropoulos, N. Konofaos, A. Iliadis, D. Davazoglou, Appl. Phys. Lett. 98 (2011) 123301.
[11] M. Vasilopoulou, A.M. Douvas, D.G. Georgiadou, L.C. Palilis, S. Kennou, L. Sygellou, A. Soultati, I. Kostis, G. Papadimitropoulos, D. Davazoglou, P. Argitis, J. Am. Chem. Soc. 134 (2012) 16178.
[12] Irfan, H. Gao, D.Y. Kim, J. Subbiah, F. So, Appl. Phys. Lett. 96 (2010) 073304.
[13] H. Ma, H.-L. Yip, F. Huang, A.K.-Y. Jen, Adv. Funct. Mater. 20 (2010) 1371.
[14] T. Matsushima, Y. Kinoshita, H. Murata, Appl. Phys. Lett. 91 (2007) 253504.

[15] P.G. Dickens, S. Crouch-Baker, M.T. Weller, Solid State Ionics 18/19 (1986) 89.
[16] S. Braun, W.R. Salaneck, M. Fahlman, Adv. Mater. 21 (2009) 1450.
[17] M.T. Greiner, M.G. Helander, Z.B. Wang, W.M. Tang, J. Qiu, Z.H. Lu, Appl. Phys. Lett. 96 (2010) 213302.
[18] A. Buckley, D. Pickup, C. Yates, Y. Zhao, D. Lidzey, J. Appl. Phys. 109 (2011) 084509.
[19] P.-S. Wang, I.-W. Wu, W.-H. Tseng, M.-H. Cheng, C.-I. Wu, Appl. Phys. Lett. 98 (2011) 173302.
[20] Y. Sun, C.J. Takacs, S.R. Cowan, J.H. Seo, X. Gong, A. Roy, Heeger, Adv. Mater. 23 (2011) 2226.
[21] Y. Sun, G.C. Welch, W.L. Leong, C.G. Takacs, G.C. Bazan, A.J. Heeger, Nat. Mater. 11 (2012) 44.
[22] S.Y. Chiam, B. Dasgupta, D. Soler, M.Y. Leung, H. Liu, Z.E. Ooi, L.M. Wong, C.Y. Jiang, K.L. Chang, J. Zhang, Sol. Energy Mater. Sol. Cells 99 (197) (2012).
[23] M. Vasilopoulou, L.C. Paillis, D.G. Georgiadou, A.M. Douvas, P. Argitis, S. Kennou, L. Syggelou, G. Papadimitropoulos, I. Kostis, N.A. Stathopoulos, D. Davazoglou, Adv. Funct. Mater. 21 (2011) 1489.
[24] G. Papadimitropoulos, N. Vourdas, K. Giannakopoulos, M. Vasilopoulou, D. Davazoglou, J. Appl. Phys. 109 (2011) 103527.
[25] N. Vourdas, G. Papadimitropoulos, I. Kostis, M. Vasilopoulou, D. Davazoglou, Thin Solid Films 520 (2012) 3614.
[26] L.C. Palilis, M. Vasilopoulou, D.G. Georgiadou, P. Argitis, Org. Electron. 11 (2010) 1887.
[27] L.C. Palilis, M. Vasilopoulou, A.M. Douvas, D.G. Georgiadou, S. Kennou, N.A. Stathopoulos, V. Constantoudis, P. Argitis, Sol. Energy Mater. Sol. Cells 114 (2013) 205.
[28] K.J. Eda, Solid State Chem. 83 (1989) 292.
[29] K.J. Eda, Solid State Chem. 98 (1992) 350.
[30] K.J. Eda, Solid State Chem. 95 (1991) 64.
[31] M.F. Daniel, B. Desbat, J.C. Lassegues, B. Gerand, M. Figlarz, Solid State Ionics 67 (1987) 235.
[32] C.J. Wright, J. Solid State Chem. 20 (1977) 89.
[33] V. Shrotriya, G. Li, Y. Yao, C.-W. Chu, Y. Yang, Appl. Phys. Lett. 88 (2006) 073508.
[34] S.R. Hammond, J. Meyer, N.E. Widjonarko, P.F. Ndione, A.K. Sigdel, A. Garcia, A. Miedaner, M.T. Lloyd, A. Kahn, D.S. Ginley, J.J. Berry, D.C. Olson, J. Mater. Chem. 22 (2012) 3249.
[35] K. Zilberberg, H. Gharbi, A. Behrendt, S. Trost, T. Riedl, ACS Appl. Mater. Interfaces 4 (2012) 1164.